

# Neuromorphic Visual Scene Understanding with Resonator Networks

Alpha Renner,<sup>1,\*</sup> Lazar Supic,<sup>2</sup> Andreea Danielescu,<sup>2</sup> Giacomo Indiveri,<sup>1</sup> Bruno A. Olshausen,<sup>3</sup> Yulia Sandamirskaya,<sup>4</sup> Friedrich T. Sommer,<sup>3,4,†</sup> and E. Paxon Frady<sup>4,‡</sup>

<sup>1</sup>*Institute of Neuroinformatics, University of Zurich and ETH Zurich, Switzerland*

<sup>2</sup>*Accenture Labs, San Francisco*

<sup>3</sup>*Redwood Center for Theoretical Neuroscience, UC Berkeley*

<sup>4</sup>*Intel Neuromorphic Computing Lab*

Inferring the position of objects and their rigid transformations is still an open problem in visual scene understanding. Here we propose a neuromorphic solution that utilizes an efficient factorization network based on three key concepts: (1) a computational framework based on Vector Symbolic Architectures (VSA) with complex-valued vectors; (2) the design of Hierarchical Resonator Networks (HRN) to deal with the non-commutative nature of translation and rotation in visual scenes, when both are used in combination; (3) the design of a multi-compartment spiking phasor neuron model for implementing complex-valued vector binding on neuromorphic hardware. The VSA framework uses vector binding operations to produce generative image models in which binding acts as the equivariant operation for geometric transformations. A scene can therefore be described as a sum of vector products, which in turn can be efficiently factorized by a resonator network to infer objects and their poses. The HRN enables the definition of a partitioned architecture in which vector binding is equivariant for horizontal and vertical translation within one partition and for rotation and scaling within the other partition. The spiking neuron model allows mapping the resonator network onto efficient and low-power neuromorphic hardware. In this work, we demonstrate our approach using synthetic scenes composed of simple 2D shapes undergoing rigid geometric transformations and color changes. A companion paper demonstrates this approach in real-world application scenarios for machine vision and robotics.

## INTRODUCTION

Visual scene understanding is a long-standing problem of machine vision and artificial intelligence. It is a notoriously hard – and largely unsolved – computational problem, as it requires searching over a very large space of possible configurations for how objects may be combined along with variations in pose, color, lighting, and other features. Convolutional artificial neural networks have been proposed as a possible approach to solving this problem. However, this approach typically requires large amounts of training data as well as additional augmentations of the data to handle variations in pose or style. Furthermore, even with these training expedients, their performance is often brittle [1, 2] and easily fooled by both artificial and real-world imagery [3, 4]. Of more concern from an engineering and security standpoint is the fact that their operation is opaque because the factors of variation in visual scenes are entangled in complicated ways via their typically large number of parameters. This makes it difficult to trace information flow and understand the system sufficiently well to fix the failure modes.

It has long been proposed that the brain solves the visual scene understanding problem via “analysis by synthesis” whereby a generative model that holds knowledge of scene components and their combinations is used to infer the components of a scene based on how well they explain the image data [5–7]. However, inference in these models can require many iterations to converge, and the high computational cost associated with these operations has prevented their widespread deployment. Recent work has shown that for such workloads –that require recurrent iterative computations– *neuromorphic computing* can vastly outperform CPU and GPU-based approaches [8]. Specifically, custom spike-based neuromorphic chips [8–12] accelerate computing times and reduce power consumption figures thanks to their parallelism, in-memory processing [13], sparsity, and event-based [14] nature. To leverage this advantage of neuromorphic hardware for scene understanding, we use a programming framework that offers an explicit binding operation, thereby overcoming the so-called feature binding problem in conventional artificial neural networks [15–17]. For example, in convolutional networks, processing image data through a cascade of linear filtering, thresholding, and pooling operations discards the binding between features, objects, and their transformations. This results in representations that are sufficient to pass certain classification benchmarks but which are easily confused when tested more rigorously, e.g., [18].

\* [alpren@ini.uzh.ch](mailto:alpren@ini.uzh.ch)

† [fsommer@berkeley.edu](mailto:fsommer@berkeley.edu)

‡ [e.paxon.frady@intel.com](mailto:e.paxon.frady@intel.com)

Our neuromorphic approach to scene analysis is based on a programming framework stemming from Cognitive Science that represents symbols or variables as high-dimensional vectors and then computes on these representations via an explicit algebra consisting of addition, multiplication, and permutation [19–21]. Models of this type are now referred to as Vector Symbolic Architectures (VSAs) [22], or Hyperdimensional Computing (HC) [23], and lately, they have been proposed as a powerful algorithmic framework for emerging computing fabrics that exhibit non-deterministic behavior at small scales and low power [24]. Here we leverage results based on VSA and HC to design a neuromorphic algorithm for scene analysis: 1) a mathematical framework that extends VSAs to represent continuous variables and functions [25], and 2) a *resonator network* that efficiently solves multi-factor vector factorization in VSAs [26, 27]. The first development enables us to encode an image in a VSA representation such that binding (vector multiplication) acts as the equivariant operation for specific geometric transformations [25], while the second one makes it tractable to infer objects and their transformations via vector factorization [26, 27].

The approach proposed falls within the larger family of multilinear models for inferring object shapes and their transformations in the context of a generative image model. These include early proposals by Pitts & McCulloch (1947)[28] and Hinton (1981)[29] for remapping sensory information into a canonical reference frame, neurobiological models such as dynamic routing [30], map-seeking circuits [31, 32], as well as bilinear models that learn to disentangle form vs. motion (or ‘style’ vs. ‘content’) [33–37]. In the particular case of bilinear models, the generative network is mathematically formulated as a tensor product. This tensor operation is, in fact, closely related to the VSA binding operation used here [38].

The paper is organized as follows. First, we describe how an image can be encoded in a VSA representation so that the binding operation is the equivariant operation for translation. With the same encoding scheme, we then formulate a generative model of a scene composed of translated template shapes and show how resonator networks [26] can infer translations and object templates that generated a given image. Extending this approach, we develop an algorithm for analyzing scenes composed of arbitrary rigid transforms of shape templates. The algorithm is based on a resonator network with a novel architecture, the *hierarchical resonator network*. Finally, we demonstrate how to implement the essential components of the hierarchical resonator network on Intel’s neuromorphic research chip, Loihi [39], utilizing an efficient spike-timing code.

## REPRESENTING IMAGES IN HYPERVECTORS

Random vectors with independent identically distributed (i.i.d.) components in high-dimensional vector spaces are very close to orthogonal with a small inner product. VSAs leverage this separation and represent individual symbols by such i.i.d. random vectors ( $\mathbf{a}, \mathbf{b}$ , etc.) in an  $N$ -dimensional space [19, 23]. More recently, VSAs have been generalized to Vector Function Architectures (VFAs) [25] that can represent not only discrete symbols but also functions [25] and real-valued quantities [40, 41]. VSAs and VFAs typically offer two complementary dyadic vector operations, superposition and binding/unbinding, which preserve the vector dimension. The  $N$ -dimensional vectors representing atomic and composite data structures during a computation are called *hypervectors*. During computation, the execution of vector operations is interleaved with parsing/decoding and error correction, exploiting similarity-based access of the interpretable hypervectors stored in the so-called *codebook*, for example, through nearest-neighbor search or auto-associative content-addressable memory [42, 43].

Here we use Fourier Holographic Reduced Representations (FHRR) [19, 44], a VSA whose atomic hypervectors are composed of phasors, i.e., complex-valued variables with unit amplitude. Similarity between two FHRR hypervectors is measured by the real part of the normalized inner product,  $\frac{1}{N} \Re(\mathbf{a}^\dagger \mathbf{b})$ , where  $\mathbf{a}^\dagger$  is the complex conjugate vector transpose. The binding operation in FHRR is the Hadamard product or component-wise multiplication  $\odot$ , with  $\mathbf{a} \odot \mathbf{b}$  for *binding*, and  $\mathbf{a} \odot \mathbf{b}^*$  for *unbinding*, where  $\mathbf{b}^*$  is the complex conjugate. The *superposition* operation is vector summation,  $\mathbf{a} + \mathbf{b}$ .

To encode an image as a hypervector, VFA index vectors are created to encode pixel location. We choose two fixed complex-valued FHRR vectors  $\mathbf{h}$  (i.e.  $h_j = e^{i\phi_j}$ ,  $\phi_j \sim \mathcal{U}[0, 2\pi]$ ) and  $\mathbf{v}$ . A pixel at the Cartesian image coordinates  $x$  and  $y$  is represented by the index vector  $\mathbf{h}^x \odot \mathbf{v}^y$ . Note that the complex exponential is multi-valued, i.e.  $(e^{i\phi_j})^x = e^{x(i\phi_j + 2\pi n)} \forall n \in \mathbb{Z}$ , but we define the operation as returning only the principal value with  $n = 0$ .

Following [25], the image  $Im(x, y)$  is encoded as a function over the pixel space via the superposition of index vectors weighted by their corresponding image pixel values  $\mathbf{s} = \sum_{x,y} Im(x, y) \cdot \mathbf{h}^x \odot \mathbf{v}^y$ . This encoding is similar to the Discrete Fourier transform but with frequencies chosen randomly and not with regular spacing. Interestingly, important features of the Fourier transform, such as the convolution theorem, remain valid even with the frequencies randomized. Further, we form a codebook with random vectors for indexing the three color channels (R/G/B)  $\mathbf{G} = [\mathbf{r}, \mathbf{g}, \mathbf{b}] \in \mathbb{C}^{N \times 3}$ . The hypervector representation of a color image is then given as:

$$\mathbf{s} = \sum_{x,y,c} Im(x, y, c) \cdot \mathbf{G}_c \odot \mathbf{h}^x \odot \mathbf{v}^y =: \Phi \mathbf{I}. \quad (1)$$

The right hand side of (1) makes explicit that hypervector encoding is linear, with  $\mathbf{I} \in \mathbb{R}^{(3P_x P_y)}$  the image reshaped as a vector, and  $\Phi \in \mathbb{C}^{N \times (3P_x P_y)}$  the codebook matrix of hypervectors for each index configuration  $\{x, y, c\}$ . Conversely, decoding the image from the hypervector uses the conjugate transpose as the linear transform:  $\mathbf{I} = \frac{1}{N} \Re(\Phi^\dagger \mathbf{s})$ . Since the codebook entries are only approximately orthogonal, this introduces small amounts of noise in the image reconstruction, which can be quantified and mitigated [45]. In this context, these noise effects are minimal.

Image encoding with (1) has pivotal properties for the scene factorization algorithm we propose. Most importantly, it ensures that the *equivariant vector operation* for image translation is the binding operation, i.e.  $\mathbf{s} \odot \mathbf{h}^{\Delta x} \odot \mathbf{v}^{\Delta y}$ , which is the VFA representation of the image translated by  $\Delta x, \Delta y$ , since

$$\mathbf{s} \odot \mathbf{h}^{\Delta x} \odot \mathbf{v}^{\Delta y} = \sum_{x,y} Im(x,y) \cdot \mathbf{h}^{x+\Delta x} \odot \mathbf{v}^{y+\Delta y} = \sum_{x,y} Im(x-\Delta x, y-\Delta y) \cdot \mathbf{h}^x \odot \mathbf{v}^y. \quad (2)$$

Also, note that image translation is well-defined for continuous values of  $\Delta x, \Delta y$ , allowing the recognition of shapes shifted by fractions of a pixel.

## A GENERATIVE MODEL OF SCENES USING VSA VECTOR OPERATIONS

To demonstrate scene factorization, we focus on synthetic images of simple visual scenes composed of object templates, in our case letters, that are translated and given one of 7 colors. Multiple objects are independently generated and then added to the scene. The task of our model is to extract from an input image the identities, colors, and locations of the objects.

We can use the VFA framework to build a generative model for such simple synthetic images. The set of letter templates forms a matrix  $\mathbf{P} \in \mathbb{R}^{(P_x P_y) \times D}$ , where  $D = 26$  is the number of different templates. As in (1), templates of the letters can be encoded as hypervectors via

$$\mathbf{d}_a = \sum_{x,y} \mathbf{P}_a(x,y) \cdot \mathbf{h}^{x-\delta_x} \odot \mathbf{v}^{y-\delta_y}, \quad (3)$$

where  $\delta_x, \delta_y$  are offsets to center the pattern within its own object-centered reference frame. Each hypervector for the templates is stored in the matrix  $\mathbf{D} = \Phi \mathbf{P}$ , with  $\Phi \mathbf{P}$  containing the vectors for each pixel as described in (3).

The equivariance property of vector binding can be used to color and position a template in the scene. Furthermore, vector superposition is employed for adding different objects. The resulting generative VFA model for a synthetic scene composed of  $L$  objects is:

$$\mathbf{s} = \sum_{i=1}^L \mathbf{d}_{p_i} \odot \mathbf{h}^{x_i} \odot \mathbf{v}^{y_i} \odot \mathbf{c}_{c_i}. \quad (4)$$

In particular here, we sample each generative factor of variation  $(p_i, x_i, y_i, c_i)$  uniformly. There are 7 colors used in the generative model given by a matrix  $\mathbf{B} \in \mathbb{R}^{3 \times 7}$  with, for instance,  $\mathbf{B}_{cyan} = [0, 1, 1]$ . The VSA codebook for colors is  $\mathbf{C} = \mathbf{G}\mathbf{B}$ .

To generate a hypervector of a synthetic scene composed of a given set of components is straightforward in the generative model (4) (see Fig. 1A for an example). For rendering the generated scene in pixel space, the hypervector can be decoded, as described earlier. Conversely, inference in the generative model (4) requires that each generative factor is represented by sufficiently dissimilar hypervectors, even if the corresponding elements in the image domain are correlated, for example, shape templates with large overlap, like “c” versus “o”.

Decorrelated hypervectors can be produced by “learning” whitened versions of the generative factors by using singular value decomposition [46]. For example, the letter templates are decomposed by singular value decomposition,  $\mathbf{P} = \mathbf{U}\Sigma\mathbf{V}$ . The whitened templates  $\hat{\mathbf{P}} = \mathbf{U}\mathbf{V}$  are encoded into hypervectors similar to (3) and stored in the codebook  $\hat{\mathbf{D}} = \Phi \hat{\mathbf{P}}$ . A similar whitening procedure is done for generating the codebook for color,  $\hat{\mathbf{C}} \in \mathbb{C}^{N \times 7}$ .

## INFERENCE WITH THE RESONATOR NETWORK

A generative model (4) with decorrelated hypervectors enables inference for a given input image, but inference in generative models is computationally expensive [47] as it involves a combinatorial search across all templates in all possible poses. Conveniently, the VSA formulation (4) permits fast parallel implementations of this search. A given synthetic pixel image to be analyzed is first transformed by (1) into a hypervector  $\mathbf{s}$ .

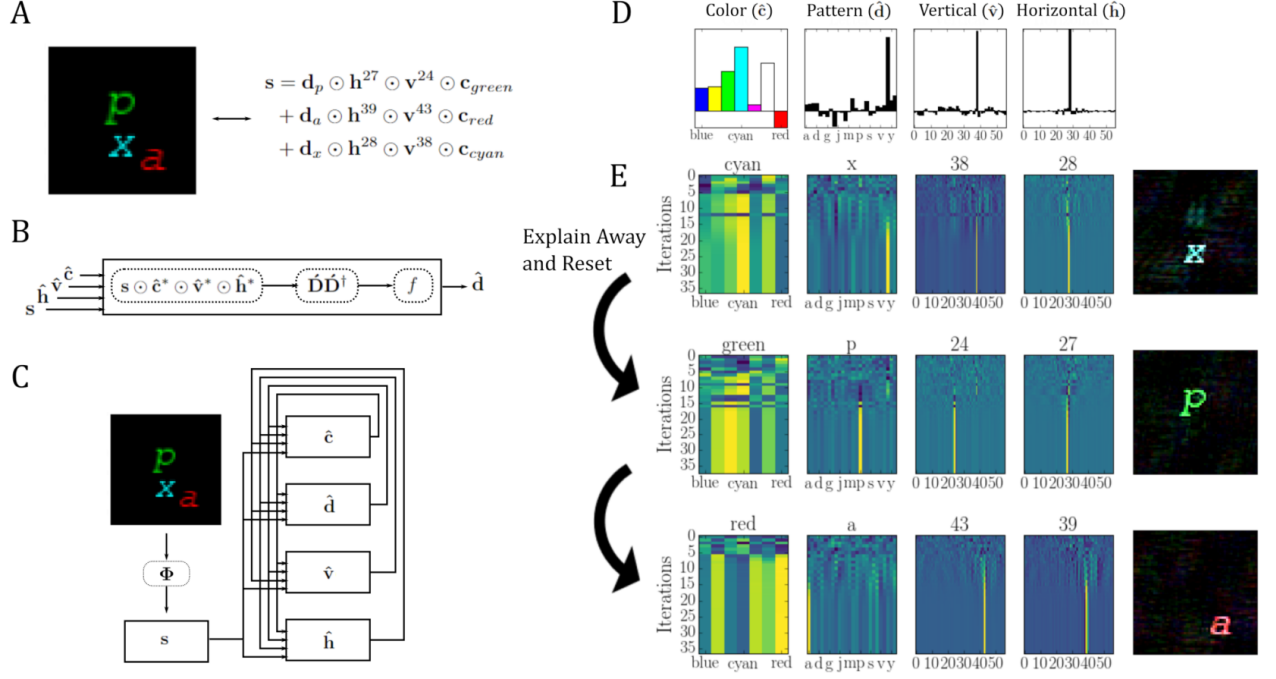


FIG. 1. Resonator network for inferring shape, color, and translation. **A.** A synthetic scene and the VSA representation of the generative model. **B.** A resonator module consists of a binding stage, a clean-up stage, and an activation function. **C.** An input scene created by the generative model is encoded into the VSA space and is the input into the resonator network. The resonator modules communicate their estimates for each factor of variation in the generative model. **C.** The weighted factor estimates in each resonator module can be decoded using the codebooks, and the maximum value is taken as the output. **D.** The four dynamic estimates in the resonator network are each visualized as a heatmap, with time represented vertically and each component represented horizontally. After several iterations, the resonator network converges to a solution and remains stable. Once converged, the component with the largest weight is chosen as the output (top of each panel). The decoded output is visualized to the right of each row. The object is then ‘explained away’ by subtracting the resonator’s estimate from the scene vector. The resonator circuit is reset and converges to another solution, which describes a different object in the scene (rows 2 and 3).

Inference of the image content then involves fitting the input vector  $s$  by the best matching templates and transforms contained in the model. Mathematically, this corresponds to a constrained optimization problem, where the optimization constraints are the valid code vectors for shape, position and color in (4). In particular, each term of the sum in (4) represents an image component formed by the product of hypervectors that encode object class, color, and pose. Thus, inference essentially is the factorization of  $s$  into specific hypervectors that satisfy the optimization constraints.

This kind of vector factorization problem is very common in VSA algorithms, and recurrent resonator networks have been proposed to solve it efficiently [26, 27]. For inference in (4), one constructs the resonator network based on inverting the generative model. The network contains one resonator module that produces an estimate for each factor in the generative model. In each iteration, a module combines all currently available information to update the estimate of its own factor and sends it to the other modules. The available information includes the input vector  $s$ , current guesses of all other factors from the other modules, and the codebook for its own set of factors.

A resonator network module contains three stages: a VSA binding stage, a linear transform, and a component-wise saturation function or normalization (Fig. 1B). The resonator network (5) solves the inference problem dynamically. Starting from random seeds, in each iteration, a module decodes its own factor from  $s$  by unbinding the estimates from all other modules. The decoded vector is then compared to the valid code vectors that are stored in a linear associative memory. Based on vector similarity, the memory *cleans up* the decoded vector to resemble one or a superposition of valid codebook vectors. After applying the transfer function  $f$ , the new estimate is sent to the other modules.

For inference in (4), the dynamic equations of the resonator network are:

$$\begin{aligned}
\hat{\mathbf{c}}(t+1) &= f\left(\hat{\mathbf{C}}\hat{\mathbf{C}}^\dagger\left(\mathbf{s} \odot \hat{\mathbf{d}}^*(t) \odot \hat{\mathbf{v}}^*(t) \odot \hat{\mathbf{h}}^*(t)\right)\right), \\
\hat{\mathbf{d}}(t+1) &= f\left(\hat{\mathbf{D}}\hat{\mathbf{D}}^\dagger\left(\mathbf{s} \odot \hat{\mathbf{c}}^*(t) \odot \hat{\mathbf{v}}^*(t) \odot \hat{\mathbf{h}}^*(t)\right)\right), \\
\hat{\mathbf{v}}(t+1) &= f\left(\hat{\mathbf{V}}\hat{\mathbf{V}}^\dagger\left(\mathbf{s} \odot \hat{\mathbf{d}}^*(t) \odot \hat{\mathbf{c}}^*(t) \odot \hat{\mathbf{h}}^*(t)\right)\right), \\
\hat{\mathbf{h}}(t+1) &= f\left(\hat{\mathbf{H}}\hat{\mathbf{H}}^\dagger\left(\mathbf{s} \odot \hat{\mathbf{d}}^*(t) \odot \hat{\mathbf{v}}^*(t) \odot \hat{\mathbf{c}}^*(t)\right)\right),
\end{aligned} \tag{5}$$

with  $f(x) = x/|x|$  and  $\mathbf{V}, \mathbf{H}$  the codebooks of uncorrelated vectors representing vertical and horizontal coordinates of pixels. A linear transform of the form  $\mathbf{V}\mathbf{V}^\dagger$  is essentially a linear auto-associative memory [48] that aligns the output to the vectors nearest to the input, stored in  $\mathbf{V}$ .

This distributed dynamic process successively improves the joint estimate of all factors (Fig. 1C). Importantly, individual modules do not settle immediately at a single estimate for their factor (like in a Hopfield memory network). In early iteration steps, they produce a superposition of many possible factors, which enables parallel search through the combinatoric solution space. In the later iterations, the interaction between modules narrows the search down to a single estimate of the identity, pose, and color of one scene component, and the network converges to a stable equilibrium (Fig. 1D, E). To analyze other scene components, the previously identified components are subtracted from  $\mathbf{s}$ , similar to “explaining away” or “deflation.”

## INFERRING ROTATION AND SCALE TRANSFORMS

The approach can easily be extended to scenes where a centered object is transformed by rotation and scaling. We will use the fact that rotation and scaling in Cartesian space becomes translation in log-polar space (Fig. 2 A), with  $\mathbf{L} \in \mathbb{R}^{L_m L_r \times P_x P_y}$  the log-polar transform matrix. Thus in log-polar coordinates, the binding operation becomes the equivariant transform for rotation and scaling. From a generative model of rotated and scaled object templates in log-polar coordinates, we can construct the following resonator network (Fig. 2 B):

$$\begin{aligned}
\hat{\mathbf{d}}(t+1) &= f\left(\hat{\mathbf{D}}_{\mathbf{L}}\hat{\mathbf{D}}_{\mathbf{L}}^\dagger\left(\mathbf{s}_{\mathbf{L}} \odot \hat{\mathbf{r}}^*(t) \odot \hat{\mathbf{m}}^*(t)\right)\right), \\
\hat{\mathbf{r}}(t+1) &= f\left(\mathbf{R}\mathbf{R}^\dagger\left(\mathbf{s}_{\mathbf{L}} \odot \hat{\mathbf{d}}^*(t) \odot \hat{\mathbf{m}}^*(t)\right)\right), \\
\hat{\mathbf{m}}(t+1) &= f\left(\mathbf{M}\mathbf{M}^\dagger\left(\mathbf{s}_{\mathbf{L}} \odot \hat{\mathbf{d}}^*(t) \odot \hat{\mathbf{r}}^*(t)\right)\right).
\end{aligned} \tag{6}$$

Here the codebooks  $\mathbf{R}$  and  $\mathbf{M}$  contain the vector symbols for each log-polar coordinate, e.g.  $\mathbf{R} = [\mathbf{r}^1, \mathbf{r}^2, \dots, \mathbf{r}^{L_r}]$ ,  $\mathbf{M} = [\mathbf{m}^1, \mathbf{m}^2, \dots, \mathbf{m}^{L_m}]$ . The codebook  $\hat{\mathbf{D}}_{\mathbf{L}} \in \mathbb{C}^{N \times L_m L_r}$  contains the bindings of these index hypervectors for log-polar coordinates akin to  $\hat{\Phi}$  (3). Further, the index vector  $\mathbf{r}$  is designed with a toroidal similarity structure, such that translated pixels wrap around the image. This is achieved by constraining the phases of  $\mathbf{r}$  to the  $N^{th}$  roots of unity like in a Fourier transform [25]. Similarly, the codebook  $\hat{\mathbf{D}}_{\mathbf{L}} = \hat{\Phi}_{\mathbf{L}}\mathbf{L}\hat{\mathbf{D}}$  contains the whitened letter patterns in the log-polar space.

Figure 2 displays an example of inference with the resonator network (6) of an image. The simulation results highlight a general problem of using generative models for analyzing a scene. Often, image components can have more than one valid explanation because of inherent symmetries. In this case, different letter templates can become identical when rotated by different angles, such as ‘b’ and ‘q’. Thus, the analysis of scenes with these letters becomes ambiguous. For ambiguous inputs, the resonator network selects one solution but will not indicate the existence of alternative solutions. Which of the solutions is selected depends on random initialization and other noise sources (Fig. 2D).

## ANALYZING SCENES COMPOSED FROM RIGID, NON-COMMUTATIVE TRANSFORMS

The next step toward analyzing realistic scenes is the ability to identify object templates transformed by arbitrary rigid transforms, including translation, rotation, scale, and color. We will describe a resonator network with a novel architecture for solving this type of image analysis.

The generative model of an image synthesized from rigid transforms of shape templates can be written as:

$$\mathbf{s} = \sum_i \mathbf{c}_{c_i} \odot \mathbf{h}^{x_i} \odot \mathbf{v}^{y_i} \odot \mathbf{\Lambda}^{-1}(\mathbf{r}^{r_i} \odot \mathbf{m}^{m_i} \odot \mathbf{d}_{p_i}), \tag{7}$$



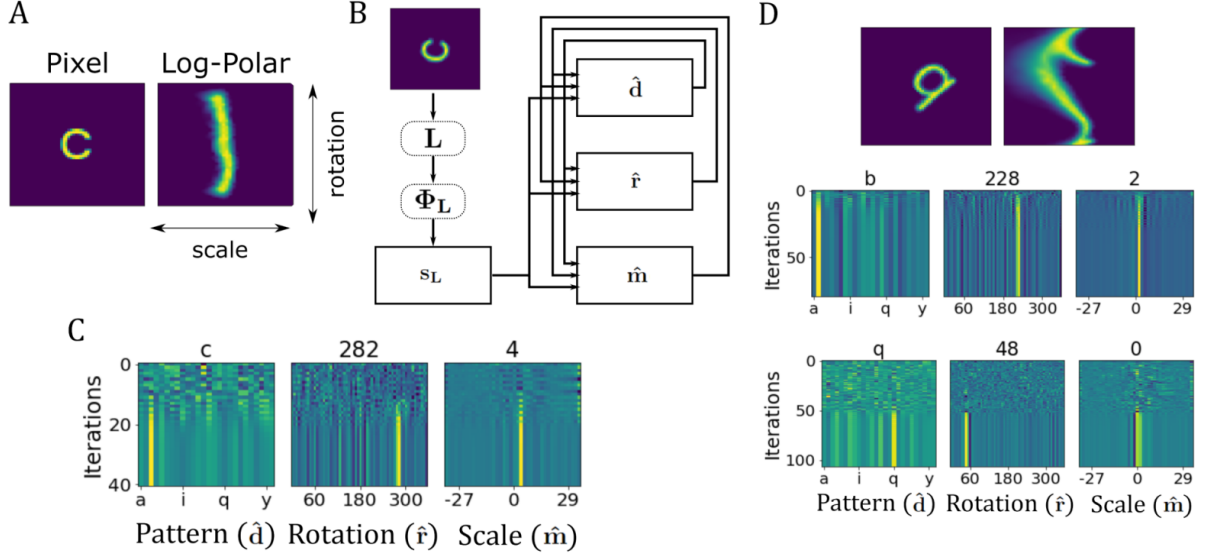


FIG. 2. Resonator network for rotation and scale. **A**. Translation in log-polar space results in rotation and scaling in Cartesian space. **B**. Diagram of resonator network for inferring shape, rotation, and scaling of input images. **C**. Example of network dynamics. **D**. Symmetries of the template lead to ambiguous factorizations. Two examples of the resonator network are shown with different random initializations. The resonator network will converge to one of the ambiguous factorizations (letters ‘b’ or ‘q’).

where  $\Lambda = \Phi_L \mathbf{L} \Phi^\dagger$  is the log-polar transform matrix in the high-dimensional VSA space. For performing inference in this generative model, one can again construct a corresponding resonator network. Describing the six factors in (7), the network consists of six fully connected factor modules that all require coordinate transforms,  $\Lambda$  or  $\Lambda^{-1}$ , in their binding stages, see Methods (10). Interestingly, the structure of these equations suggests a partitioned network architecture that avoids redundant coordinate transforms. The final network consists of two partitions, each fully connected internally: one operating in Cartesian and one in log-polar coordinates. Each partition has an additional module that serves as the communication bridge between the partitions. Conveniently, the bridge modules have exactly the same internal stages as other resonator modules, a binding stage followed by a linear transform ( $f$  is the identity function in this case):

$$\hat{\mathbf{l}}(t+1) = \Lambda^{-1}(\hat{\mathbf{r}}(t) \odot \hat{\mathbf{m}}(t) \odot \hat{\mathbf{d}}(t)), \quad (8)$$

$$\hat{\mathbf{p}}(t+1) = \Lambda(\mathbf{s} \odot \hat{\mathbf{c}}^*(t) \odot \hat{\mathbf{h}}^*(t) \odot \hat{\mathbf{v}}^*(t)). \quad (9)$$

En lieu of writing the entire equation system, we describe the schematic of the partitioned resonator network in Fig. 3A and its relations to the resonator networks (6) and (5). The *log-polar partition*, the right column of modules in Fig. 3A, contains the “top-down” bridge module (8) and the modules from (6). The top-down bridge module (8) produces  $\hat{\mathbf{l}}$ , the estimate of a rotated and scaled shape computed by the log-polar partition, transformed to Cartesian coordinates. The *Cartesian partition*, the left column of modules in Fig. 3A, contains the modules from (5), but the module with output  $\hat{\mathbf{d}}$  replaced by the “bottom-up” bridge module (9). The previous input from  $\hat{\mathbf{d}}$ , which is an estimate of the letter shape, is replaced by the top-down signal  $\hat{\mathbf{l}}$ , which is an estimate of the letter shape with a particular rotation and rescaling. The bottom-up bridge unit (9) produces  $\hat{\mathbf{p}}$ , which removes the estimated translation and coloring from the input and transforms a centered version of the input into log-polar coordinates. This in effect replaces the input for (6).

We call the architecture in Fig. 3A the *hierarchical resonator network* because the bidirectionally connected partitions assume different hierarchy levels by the definition of Felleman and Van Essen [49]. The Cartesian partition receives direct input according to a lower level, while the log-polar partition is one removed from the sensory input according to a higher level. The log-polar partition also holds the discrete shape templates in memory, the arguably most abstract aspect of the image components.

A successful example of inference with the hierarchical resonator network is shown in Fig. 3B. The upper row shows a factorization process, revealing the letter “k”, and the lower row shows a second factorization process, revealing the letter “m”. Note how the estimates of all factors are undecided and blurry in early iteration steps and become sharp quite suddenly during iteration. An unsuccessful example of inference is shown in Fig. 4. In this case, the first factorization falsely explains the arched portion of the “m” with a rotated “s”. After subtraction of the “s” there

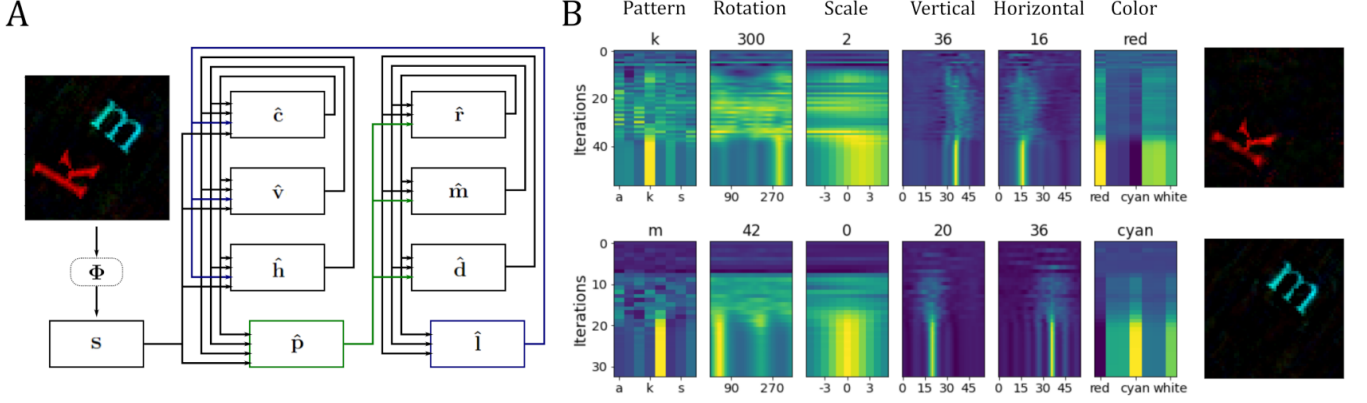


FIG. 3. The hierarchical resonator network for inferring rigid transforms. **A.** Schematic diagram of the hierarchical resonator network. **B.** The dynamics of the resonator network identifying objects in the input scene.

are still parts of the “m” left, which the second factorization run falsely explains as an “a”. This failure in analyzing one image component would probably not prevent a third factorization run from correctly identifying the second image component as a “k” (experiment not shown). However, even though these examples did not find the true generative factor, the explanations still have significant correlations with the input. In the supplement, we describe some modifications to the resonator network dynamics that mitigate these errors, such as adding non-linearities that encourage sparse solutions. However, these modifications cannot completely eliminate this issue which our model shares with other generative model approaches, e.g., [31].

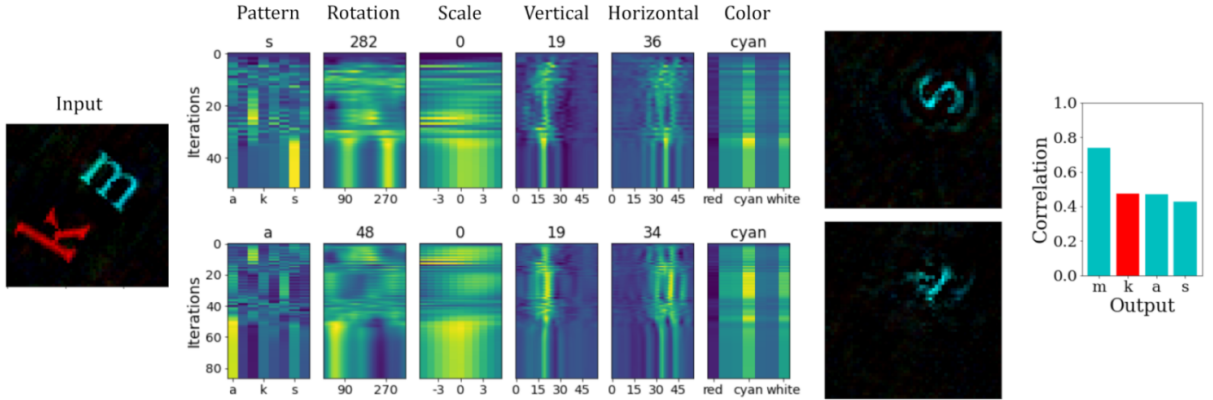


FIG. 4. Local minima in the hierarchical resonator network. Often the network converges to solutions where a shape is incorrectly fit into the explanation of the scene. Note how there are multiple peaks in some of the factors, which induces complicated overlaps of stored patterns. However, correlations between these incorrect explanations and the input are on par with the correct explanations (right panel).

## IMPLEMENTATION WITH SPIKE-TIMING-BASED PHASOR NEURONS

Finally, we implement the core elements of our model for visual scene analysis as an SNN with an efficient spike-timing code running on Intel’s Loihi neuromorphic research chip [39]. As a proof of concept, we only include the factors for translation ( $\hat{h}$ ,  $\hat{v}$ ) and the pattern ( $\hat{d}$ ) of the equation system (10), see Fig. 5A. The components of the complex VFA vectors are represented by the spike timing of integrate and fire neurons [50]. Specifically, the spike time within a predefined cycle window of length  $T$  represents the phase of a complex number (see Fig. 5B). Conveniently in (10), magnitudes of complex numbers do not have to be represented, as the non-linear function  $f$  is the phasor-projection, and the binding operation does not change phasor magnitudes.

The SNN resonator network on Loihi consists of 3-factor modules that are connected recurrently, as shown in Fig. 5.

The input spike generator converts the input vector  $\mathbf{s}$  into spikes and transmits these spikes into the binding stages of the modules (Fig. 5B). Each binding stage performs a neuron-wise complex phase shift based on its inputs (Fig. 5C), implementing the FHRR binding operation. The cleanup module (Fig. 5D) performs a matrix multiplication with the auto-associative matrix, e.g.,  $\mathbf{H}\mathbf{H}^\dagger$ . An additional gate stage in each module controls the flow of spikes through the network, making sure that the network maintains the correct timing.

To implement phase addition in FHRR binding, the spike delay of a neuron has to represent the sum of spike delays of two inputs. Input-dependent firing delays can be achieved on Loihi through a multi-compartment integrate-and-fire model (Fig. 5B). Two of the compartments, “aux” and “soma”, act like clocks with a cycle time of  $T$  by simply integrating constant inputs and resetting when they reach a threshold. The first input ( $\mathbf{s}$ ) to the “soma” compartment resets the soma’s clock. The second input acts as a gate from the aux neuron to the dendrite. When the gate is opened by the second input spike, the aux state is added to the soma state, delaying the soma from reaching the spike threshold and thus shifting the timing of the output spike (as illustrated in Fig. 5C). Note that this implementation of phase addition is specific to the Loihi hardware.

The complex-valued matrix-vector product is implemented through synaptic connections with time delays representing the phase of the synaptic weights (Fig. 5D). The summation of complex numbers corresponds to the integration of sine waves [50]. On Loihi, we combine inhibitory currents with a delayed excitatory current evoked by each input spike to create an approximate sine wave in the membrane potential. This mechanism is illustrated for just 2 inputs in Fig. 5E, but the approximation becomes more robust with more input neurons.

After the cleanup, the spikes representing each factor are fed back to the binding stage. The input to the binding stage has to be timed correctly because the shift module needs multiple cycles for its computation. To provide proper timing, the gate stage between modules blocks all spikes until it is opened by a regularly occurring input. The gating between pairs of neurons is implemented by a group of neurons with an inhibitory bias current that prevents spiking, which is counteracted by disinhibition when the gate is opened for one cycle. One iteration in the resonator network takes in total 5 cycles on Loihi. In our experiment (Fig. 5), we set the cycle time  $T = 16$  timesteps, i.e. the phasors have 16 discrete phases.

Fig. 6 shows a comparison between Loihi and a CPU in terms of energy and latency. While Loihi is slower, it is orders of magnitude more energy efficient (Fig. 6A and B). For the largest network size, Loihi is 171 times more efficient in terms of energy-delay-product (Fig. 6C) and scales better than the CPU for increasing network size, likely due to sparse, event-based matrix multiplication. The comparison uses cleanup with a full  $N \times N$  auto-associative matrix on both Loihi and the CPU. For small numbers of symbols, it is computationally advantageous to first multiply with the decoding matrix (e.g.,  $\mathbf{H}^\dagger$ ) and then with the encoding matrix ( $\mathbf{H}$ ). The intermediate result can, however, not be represented in a phasor encoding without amplitudes. We are working on an encoding that is able to represent amplitudes on Loihi 2, the next generation of the Loihi chip, which will improve the scalability of the architecture.

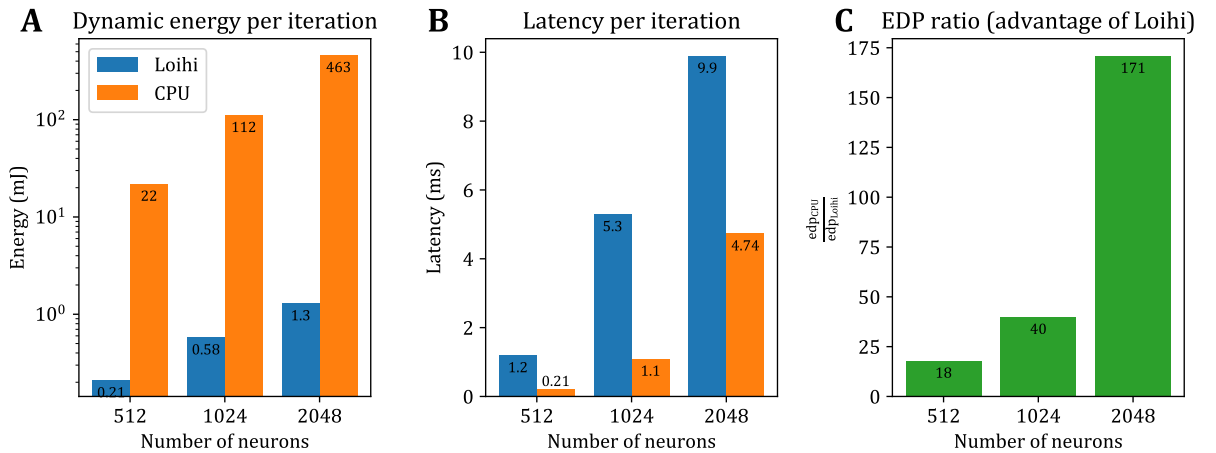


FIG. 6. **A.** Logarithmic plot of the dynamic energy per iteration of the resonator with three factors on Loihi and a CPU for different network sizes (number of elements of the VSA vectors). **B.** Time used for one iteration of the resonator on Loihi and a CPU **C.** Energy-delay-product (EDP) of the CPU divided by the EDP of Loihi. Loihi is 41 to 266 times more efficient depending on the size of the resonator and gains an advantage for larger network sizes.



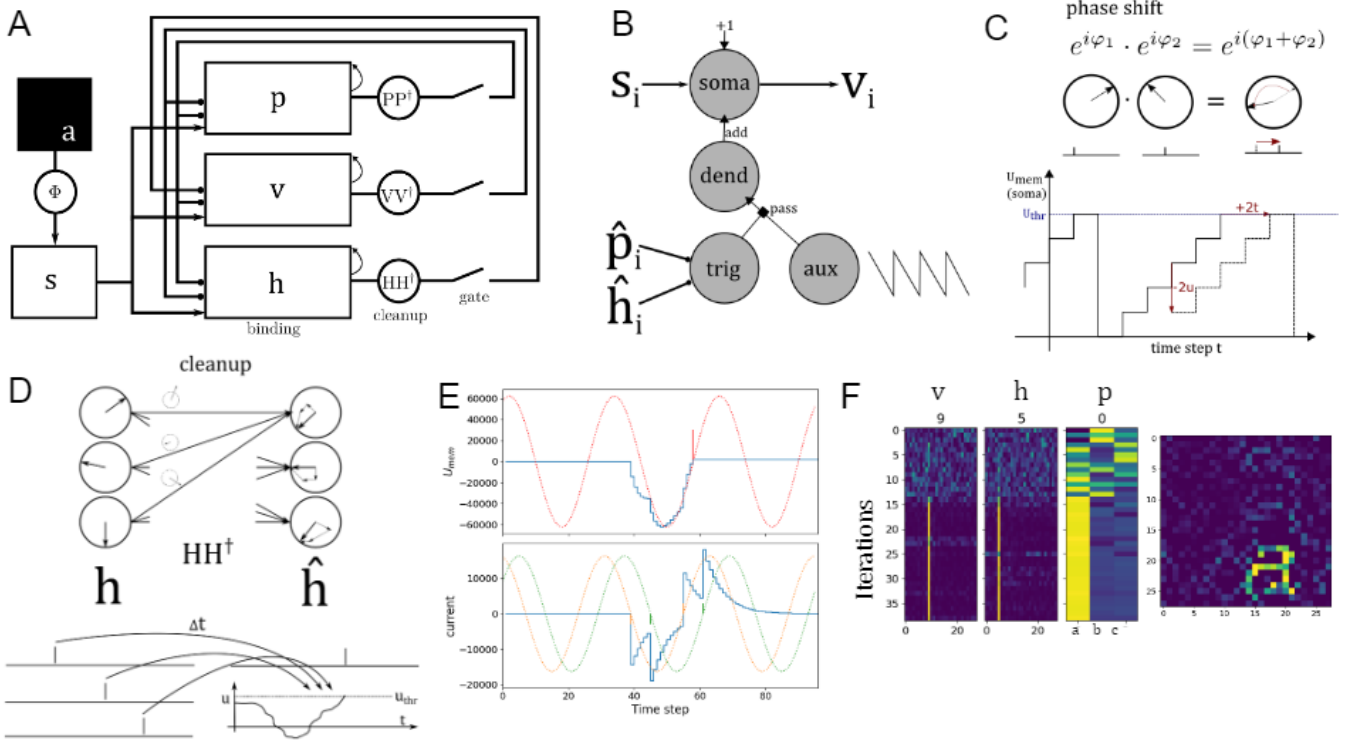


FIG. 5. The resonator network on the Loihi neuromorphic hardware with phasor integrate and fire neurons. **A.** Schematic of the resonator architecture implemented on Loihi. **B.** Implementation of the (un-)binding module (complex phase-shifting) as a 4-compartment neuron on Loihi. This is repeated for each element of the vector. Input from  $\hat{p}$  and  $\hat{h}$  triggers a “pass” operation that lets current from an auxiliary oscillating compartment flow into the dendritic compartment. The soma integrates a constant current so that the neuron fires regularly, but it can be delayed by the inhibitory input from the dendritic compartment. **C.** Mechanism of the phase shift. Here, the soma membrane potential is inhibited by 2, so it will reach the threshold two timesteps later, corresponding to a phase shift of 2. The inset at the top shows the equation of complex multiplication, its phasor representation, and the corresponding spike timing in phasor I&F neurons. **D.** Mechanism of the cleanup module. Top: Phasor representation of the complex matrix multiplication of  $h$  with the cleanup matrix  $HH^\dagger$ . Each complex matrix element corresponds to a synapse with a weight and a phase. In the receiving neuron, the weighted phases are summed up. Bottom: The same mechanism with I&F phasor neurons. Complex phases correspond to spike timing and complex synapses to synapses with a weight and a delay. This works as the complex addition can be represented as the addition of sine waves (see panel E). **E.** Mechanism of the complex adder with I&F phasor neurons. The neuron receives two inputs at different phases. Each input elicits an inhibitory postsynaptic current with a delay of  $1/2 T$  and an excitatory postsynaptic current with a delay of  $T$ . The current gets integrated into the membrane potential, which approximates a sine wave. Here, the red wave is the sum of the orange and the green wave. In blue, the membrane potential and input current of the Loihi neuron are shown. The spiking threshold is set to 0, i.e., the spike happens when the sine is changing signs. **F.** States of the resonator on Loihi over 40 iterations and reconstructed image from resonator states.

## DISCUSSION

We have described a novel algorithm for inference in generative models and its neuromorphic implementation with an efficient spike-timing code [50] on modern spiking neuromorphic hardware [39]. This algorithm is validated on the problem of analyzing synthetic visual scenes and has been used to demonstrate efficient applications to real-world task, visual odometry in robotics [51].

Our work offers a flexible programming framework for energy-efficient neuromorphic computing. The significant advantage of the VSA framework over traditional artificial neural networks (ANN) has been emphasized recently in the context of general parallel computing [52–54]. To further improve efficiency, a spatially sparse complex network (e.g., VSA models with block codes [38]) could be implemented. This would reduce spike traffic and requires less memory for codebooks. However, it comes at the cost of a more expensive binding operation [55].

Inference in generative models – also known as “analysis by synthesis” – is a powerful method for invariant pattern analysis, but it is infamously computationally expensive [47]. Our proposal to make it tractable hinges on vector

binding, an operation offered by VSAs but not by conventional neural networks, and a recent proposal of resonator networks, modular recurrent networks for efficient vector factorization [26, 27]. Three key ideas enable invariant pattern recognition with resonator networks on neuromorphic hardware. The first idea is to develop data encoding schemes and generative models that make binding the equivariant vector operation for a factor of variation, such as image translation. The second idea addresses the existence of multiple factors of variation that are non-commutative, like translation versus image rotation and scaling. Inspired by a classical method for image registration, the Fourier-Mellin transform [56–58], we propose a novel partitioned resonator network. The network consists of two partitions of fully connected modules, one operating in Cartesian, the other in log-polar coordinates, coupled by a single pair of bridge modules. Binding is the equivariant operation for translation in one partition for rotation and scaling in the other. The third idea is to use multi-compartment neuron models for implementing the complex vector binding operation in a spike-timing code on neuromorphic hardware.

Our algorithm is demonstrated on the analysis of simple synthetic scenes. It often succeeds but can also fail for several causes, most of them common to other generative model approaches. One problem is that the resonator network sometimes settles on spurious matches involving complex mixtures of generative factors. We explore the addition of sparsity mechanisms to the resonator dynamics that encourage simple scene explanations (see Methods). Another cause is mutual correlations between shape templates. While we do eliminate correlations between shape templates in a default pose, strong correlations can still arise in different relative poses. The removal of such correlations would require unsupervised learning exhaustively exploring the space of transforms, maybe akin to theories of how random sampling and unlearning during REM sleep could eliminate spurious minima in memory networks [59]. Another cause for failure is ambiguity in the input image that arises due to the presence of geometric symmetries in the shape templates. It could be possible to avoid reading a “p” as a rotated “d” by including priors, or better, contextual priors, constraining the considered rotation angles.

The concept of scene analysis by inference in generative models is by now well established [7]. However, it is only relatively recently that we have seen concrete, working neural models that probe and explore its application in practice. One such example is the map-seeking circuit (MSC) [31], a feedback multi-layer network that has been demonstrated on scene analysis and also has been successful in adaptive optics applications [60]. Our method shares with the MSC the use of superposition and content-addressable memory for estimating transforms. The main difference lies in the implementation of image transforms and how inference is computed. The MSC uses standard ANN operations, and because it lacks the vector binding operation, the search over image transforms requires large sets of fixed transform matrices tiling the transform parameter (such as the rotation angle) at sufficiently fine resolution. In the MSC, the use of each transform matrix is controlled by a non-negative continuous variable, which is dynamically adjusted by the inference process. Bilinear models [33, 34, 37] have been proposed to extract two factors of variation from an input. Bilinear models differ in that they use standard optimization methods for the computationally expensive inference procedure. These models have been demonstrated with a limitation to just two factors, mainly due to the drastic computation and memory cost of the large high-order tensors required to generalize to more factors. The work on bilinear models differs in focus – it studies how to learn the components in a generative model from input – whereas we are focusing mainly on the inference of a known generative model. However, during the learning procedure, these models propose the construction of the generative model by singular value decomposition of the input samples, which we also have adopted here.

Although developed for technical applications, our model also has implications for neuroscience. The feature binding problem of neuroscience is solved by the binding operation in VSA-type models, but original VSA models did not offer a solution to how the binding operation could be implemented by neurons of the brain. Our work suggests an efficient implementation of binding and visual perception with spiking neurons. In particular, the phasor neuron proposed for implementing binding corresponds to a velocity-controlled oscillator (VCO), which has been proposed as a model for place and grid cells [61, 62]. Without input, the neuron fires periodically, and the spike phase is constant. Input slows down the oscillation by inhibition leading to a phase shift. Thus, our model makes specific predictions about computational roles of spike timing and oscillations that can be tested in neuroscience data and experiments.

We hope our current work blazes a trail to use neuromorphic hardware for making the generative model approach in scene analysis tractable. The path towards neuromorphic analysis of naturalistic scenes, useful for embodied agents, will require revising the generative model (7), such as adding priors, 3D shape models with 3D transforms [63] and effects of occlusion [64].

## METHODS

### Details of simulation experiments

Simulation experiments using the resonator network were implemented in python. The dimensionalities used were  $N = 50,000$  in all experiments. In all experiments, the resonator network is initialized to a random state.

The full dynamic equations for the hierarchical resonator network:

$$\begin{aligned}
\hat{\mathbf{c}}(t+1) &= f\left(\hat{\mathbf{C}}\hat{\mathbf{C}}^\dagger\left(\mathbf{s} \odot \hat{\mathbf{h}}^*(t) \odot \hat{\mathbf{v}}^*(t) \odot [\Lambda^{-1}(\hat{\mathbf{r}}(t) \odot \hat{\mathbf{m}}(t) \odot \hat{\mathbf{d}}(t))]^*\right)\right), \\
\hat{\mathbf{h}}(t+1) &= f\left(\hat{\mathbf{H}}\hat{\mathbf{H}}^\dagger\left(\mathbf{s} \odot \hat{\mathbf{c}}^*(t) \odot \hat{\mathbf{v}}^*(t) \odot [\Lambda^{-1}(\hat{\mathbf{r}}(t) \odot \hat{\mathbf{m}}(t) \odot \hat{\mathbf{d}}(t))]^*\right)\right), \\
\hat{\mathbf{v}}(t+1) &= f\left(\hat{\mathbf{V}}\hat{\mathbf{V}}^\dagger\left(\mathbf{s} \odot \hat{\mathbf{c}}^*(t) \odot \hat{\mathbf{h}}^*(t) \odot [\Lambda^{-1}(\hat{\mathbf{r}}(t) \odot \hat{\mathbf{m}}(t) \odot \hat{\mathbf{d}}(t))]^*\right)\right), \\
\hat{\mathbf{d}}(t+1) &= f\left(\hat{\mathbf{D}}_L\hat{\mathbf{D}}_L^\dagger\left([\Lambda(\mathbf{s} \odot \hat{\mathbf{c}}^*(t) \odot \hat{\mathbf{h}}^*(t) \odot \hat{\mathbf{v}}^*(t))] \odot \hat{\mathbf{r}}^*(t) \odot \hat{\mathbf{m}}^*(t)\right)\right), \\
\hat{\mathbf{r}}(t+1) &= f\left(\hat{\mathbf{R}}\hat{\mathbf{R}}^\dagger\left([\Lambda(\mathbf{s} \odot \hat{\mathbf{c}}^*(t) \odot \hat{\mathbf{h}}^*(t) \odot \hat{\mathbf{v}}^*(t))] \odot \hat{\mathbf{d}}^*(t) \odot \hat{\mathbf{m}}^*(t)\right)\right), \\
\hat{\mathbf{m}}(t+1) &= f\left(\hat{\mathbf{M}}\hat{\mathbf{M}}^\dagger\left([\Lambda(\mathbf{s} \odot \hat{\mathbf{c}}^*(t) \odot \hat{\mathbf{h}}^*(t) \odot \hat{\mathbf{v}}^*(t))] \odot \hat{\mathbf{d}}^*(t) \odot \hat{\mathbf{r}}^*(t)\right)\right).
\end{aligned} \tag{10}$$

The codebooks  $\hat{\mathbf{D}}_L \in \mathbb{C}^{N \times 26}$  and  $\hat{\mathbf{C}} \in \mathbb{C}^{N \times 7}$  are formed from whitened templates projected into the high-dimensional vector space. Specifically, the templates are transformed into log-polar coordinates and decomposed by the singular value decomposition, i.e.,  $\mathbf{P}_L = \mathbf{L}\mathbf{P} = \mathbf{U}_L\mathbf{\Sigma}_L\mathbf{V}_L$ . The whitened templates are given by  $\hat{\mathbf{P}}_L = \mathbf{U}_L\mathbf{V}_L$ , which is then projected into the high-dimensional space by  $\hat{\mathbf{D}}_L = \Phi_L\hat{\mathbf{P}}_L$ . A similar procedure is done for the colors to make  $\hat{\mathbf{C}}$ .

In this model, rotation as an operation must have the correct topology for its representation – i.e., rotation by  $360^\circ$  results in the same image. This is done by ensuring that the representation vector  $\mathbf{r}$  also has circular topology. The circular topology is encoded by defining a periodic kernel for the representation  $\mathbf{r}$ , where the random phases of the components of  $\mathbf{r}$  are sampled from a discrete probability distribution [25]. Specifically, the phase circle is divided into  $L_r$  discrete samples and each component of  $\mathbf{r}$  is one of these samples,  $r_i \in \{e^{i2\pi k/L_r} \mid k \in \{1, \dots, L_r\}\}$ .

Beyond the dynamics described in equation (10), we included some modifications to improve performance. One modification included hysteresis in the update dynamics, where some fraction of the past state would be included in the next update, i.e.:

$$\mathbf{d}(t+1) = \mathbf{d}(t) + \gamma f(\hat{\mathbf{D}}\hat{\mathbf{D}}^\dagger(\mathbf{s} \odot \hat{\mathbf{h}}^*(t) \odot \hat{\mathbf{v}}^*(t))) \tag{11}$$

with  $\gamma$  controlling the rate of the hysteresis.

A second modification encouraged sparsity in the solutions by including a non-linearity during the cleanup that encourages sparsity, such as a polynomial exponent or softmax function, i.e.:

$$\mathbf{d}(t+1) = f(\hat{\mathbf{D}}p(\hat{\mathbf{D}}^\dagger(\mathbf{s} \odot \hat{\mathbf{h}}^*(t) \odot \hat{\mathbf{v}}^*(t)))) \tag{12}$$

where, for instance,  $p(\mathbf{x}) = \mathbf{x}^k/|\mathbf{x}^k|_2$ , with  $k$  typically being 2 or 3.

### Details of hardware implementation

On Loihi, we implemented a smaller model that solves a  $28 \times 28 \times 3$  factorization task. We implemented the network on Intel’s neuromorphic research chip Loihi [39]. A smaller version was implemented on the USB form factor system ”Kapoho Bay” that features two Loihi chips with a total of 256 neuro cores in which a total of 262,144 neurons and up to 260 million synapses can be implemented. The embedded x86 processors are used for monitoring and sending input spikes.

By using phasors in a spiking network, operations of multiplication and addition of complex vectors become available on the hardware. Phasors can be implemented either natively with resonate and fire neurons or with certain constraints in more commonly available integrate and fire neurons [50]. In this work, we use integrate and fire neurons with a single spike per cycle of  $T=16$  timesteps, which allows us to represent complex numbers of unit magnitude and discrete (4-bit) phase.

Each complex number that is an element of a hyperdimensional vector is implemented on the hardware as a neuron. The numbers are constrained to the unit circle in the Gaussian number plane so that the amplitude is fixed to 1. The complex phase is represented using the phasor integrate and fire neurons described by [50] as spike timing within a periodic window.

The binding operation in FHRR is the Hadamard (elementwise) product of a complex vector. Multiplication of unit complex numbers is the addition of their phases. As we represent the phases of complex numbers as spike timing, all we need to do for binding is an elementwise modulo addition of spike times. For this, a 4-compartment neuron on Loihi is used. Each Loihi compartment has two state variables  $v$ , and  $u$ , that act like a current-based integrate and fire neuron. The structure of this neuron is shown in Figure 5 and the mechanism is illustrated in Figure 5. Whenever the ‘trig’ compartment receives an input, the voltage of the ‘aux’ compartment is transferred into the ‘dend’ compartment. The ‘dend’ compartment’s voltage is added to the soma compartment and resets at each timestep.

Note that there are two versions of the binding circuit, one for binding and one for unbinding. Unbinding is element-wise multiplication with the complex conjugate (denoted by  $*$  in the equations), i.e., phases are subtracted instead of added. In the binding circuit, the ‘aux’ compartment counts down from 0 to  $-T$ ; in the unbinding circuit, the ‘aux’ compartment counts up from  $-T$  to 0. This way, the timing of the spike arriving at the ‘trig’ compartment has the opposite effect on the timing of the ‘soma’ output spike. This works as modulo  $T$  addition of  $x$  is the same as modulo  $T$  subtraction of  $T-x$ .

After the binding module, spikes are sent through a cleanup matrix. The first spikes sent out of the binding module correspond to the first input to the soma (i.e.,  $s$ ), so only in the two following cycles the binding module outputs the spikes with the correct phase shift. Therefore, there is a gate after the cleanup before spikes are sent back to the binding module. As the binding module converts all inputs into delays, only a single spike per iteration and input is allowed to be sent in. So, the gate only lets through a single spike per neuron in the third cycle, which is where the quality of the cleanup output is best. The gate module consists of an array of neurons of length  $N$  that is connected in a 1:1 manner from the cleanup module to the binding module. The gate module’s neurons are inhibited by default and only relay spikes when they are switched on by a regular input spike that brings them close to their firing threshold.

Furthermore, the gate is connected with synapses that add a constant delay to make sure that the following input to the binding module only arrives after the first input from  $s$ . By subtracting two timesteps from the delay, this delayed connection is also used to correct for the fact that each synaptic connection adds a delay of one timestep, which would bring the loop out of phase with the clock-like counter (‘aux’ compartment) in the binding module.

In order to reach better convergence, the cleanup module has a recurrent 1:1 connectivity, i.e., each neuron is connected back to itself with a delay of one cycle  $T$ . This leads to slower evolution of the resonator state over iterations. The resonate and fire neuron model, which will be available in the next version of the chip, implements this feature in its subthreshold dynamics.

Because fanout (the number of connections allowed to leave a neuron) is limited per core on the chip, we distributed neurons on several cores over the chip and pruned half of the synapses with the lowest weights from the cleanup matrix. The dense cleanup matrix is the most limiting component of the whole architecture. An alternative would be to split the cleanup matrix into its two components, reducing the number of synapses significantly in most cases. However, the layer in between the two matrix multiplications cannot be represented with a spiking phasor with unit magnitude. Graded spikes on the next version of Loihi could be used to enable phasors with a magnitude.

Power measurements for the Loihi 1 chip were obtained remotely using NxSDK version 0.9.9 on the Nahuku32 board ncl-ghrd-01. The Loihi board was interfaced to a system with an Intel Xeon CPU E5-2670 @ 2.60GHz and 128GiB of RAM running Ubuntu 20.04.4 LTS. Intel Labs provided both software API and hardware. All probes, including the output probes, except the energy probes, were deactivated. Energy was averaged over 20 iterations. Measurements for the CPU were obtained with Intel SoC Watch on a system with an Intel Core i9-7920X CPU @ 2.9GHz and 128GiB of RAM running Ubuntu 20.04 LTS. Simulations were run with Python 3.8.10 and NumPy 1.23.1. The process was constrained to use 12 threads since we found this to provide the best energy-delay-product measurement. The energy of the DRAM was not included. The latency and energy were averaged over 10000 iterations. Dynamic energy was measured by subtracting the static energy that is used when running the system without the load for the same amount of time. So dynamic energy is the energy associated with the computation and excludes leakage energy.

## ACKNOWLEDGMENTS

A.R. discloses support for the research of this work from Accenture Labs and the Swiss National Science Foundation (SNSF) [ELMA PZOOP2 168183]. G.I. discloses support for the publication of this work from SNSF [SMALL 20CH21 186999]. F.T.S. discloses support for the research of this work from NIH [1R01EB026955-01]. We thank Intel Neuromorphic Computing Lab for providing access to the Loihi hardware and related software. We thank Elvin Hajizada for running CPU power measurements.

Notation		Factors		Transforms	
$\hat{\mathbf{A}}$	Whitened codebook	$\mathbf{c} / \hat{\mathbf{C}}$	Color	$\Phi, \Phi_P, \Phi_L, \mathbf{G}$	VSA codebooks
$\hat{\mathbf{a}}$	Factor estimate	$\mathbf{h} / \mathbf{H}$	Horizontal position	$\mathbf{L} (\Lambda)$	Log-polar transform (VSA space)
$\mathbf{A}^\dagger$	Complex conjugate transpose	$\mathbf{v} / \mathbf{V}$	Vertical position	$\mathbf{s} = \Phi \mathbf{I}$	Input image
$\mathbf{a}^*$	Complex conjugate	$\mathbf{r} / \mathbf{R}$	Rotation	$\mathbf{D} = \Phi_P \mathbf{P}$	Template images
$\mathbf{a} \odot \mathbf{b}$	Binding (Hadamard Product)	$\mathbf{m} / \mathbf{M}$	Scale factor	$\mathbf{D}_L = \Lambda \mathbf{D} = \Phi_L \mathbf{L} \mathbf{P}$	Log-polar templates
$\mathbf{a} + \mathbf{b}$	Summation or superposition	$\mathbf{d} / \hat{\mathbf{D}} / \hat{\mathbf{D}}_L$	Centered template	$\mathbf{C} = \mathbf{G} \mathbf{B}$	Generative Colors
$\mathbf{a}^{-1}$	Inverse				
$\Re(a)$	Real part of complex number				

TABLE I. Notation and symbols reference

## REFERENCES

- 
- [1] C. Szegedy, W. Zaremba, I. Sutskever, J. Bruna, D. Erhan, I. Goodfellow, and R. Fergus, “Intriguing properties of neural networks,” *arXiv preprint arXiv:1312.6199*, 2013.
  - [2] A. Madry, A. Makelov, L. Schmidt, D. Tsipras, and A. Vladu, “Towards deep learning models resistant to adversarial attacks,” *arXiv preprint arXiv:1706.06083*, 2017.
  - [3] A. Nguyen, J. Yosinski, and J. Clune, “Deep neural networks are easily fooled: High confidence predictions for unrecognizable images,” in *Proceedings of the IEEE conference on computer vision and pattern recognition*, pp. 427–436, 2015.
  - [4] A. Kurakin, I. J. Goodfellow, and S. Bengio, “Adversarial examples in the physical world,” in *Artificial intelligence safety and security*, pp. 99–112, Chapman and Hall/CRC, 2018.
  - [5] D. M. MacKay, “Towards an information-flow model of human behaviour,” *British Journal of Psychology*, vol. 47, no. 1, pp. 30–43, 1956.
  - [6] U. Neisser, *Cognitive psychology*. Appleton-Century-Crofts, 1966.
  - [7] A. Yuille and D. Kersten, “Vision as bayesian inference: analysis by synthesis?,” *Trends in cognitive sciences*, vol. 10, no. 7, pp. 301–308, 2006.
  - [8] M. Davies, A. Wild, G. Orchard, Y. Sandamirskaya, G. A. F. Guerra, P. Joshi, P. Plank, and S. R. Risbud, “Advancing neuromorphic computing with loihi: A survey of results and outlook,” *Proceedings of the IEEE*, pp. 1–24, 2021.
  - [9] P. A. Merolla, J. V. Arthur, R. Alvarez-Icaza, *et al.*, “A Million Spiking-neuron Integrated Circuit with a Scalable Communication Network and Interface,” *Science*, vol. 345, no. 6197, pp. 668–673, 2014.
  - [10] S. Furber, F. Galluppi, S. Temple, and L. Plana, “The SpiNNaker project,” *Proceedings of the IEEE*, vol. 102, pp. 652–665, May 2014.
  - [11] S. Moradi, N. Qiao, F. Stefanini, and G. Indiveri, “A scalable multicore architecture with heterogeneous memory structures for dynamic neuromorphic asynchronous processors (DYNAPs),” *Biomedical Circuits and Systems, IEEE Transactions on*, vol. 12, pp. 106–122, Feb. 2018.
  - [12] J. Pei, L. Deng, S. Song, M. Zhao, Y. Zhang, S. Wu, G. Wang, Z. Zou, Z. Wu, W. He, F. Chen, N. Deng, S. Wu, Y. Wang, Y. Wu, Z. Yang, C. Ma, G. Li, W. Han, H. Li, H. Wu, R. Zhao, Y. Xie, and L. Shi, “Towards artificial general intelligence with hybrid tianjic chip architecture,” *Nature*, vol. 572, pp. 106–124, Aug. 2019.
  - [13] G. Indiveri and S.-C. Liu, “Memory and information processing in neuromorphic systems,” *Proceedings of the IEEE*, vol. 103, no. 8, pp. 1379–1397, 2015.
  - [14] G. Gallego, T. Delbruck, G. M. Orchard, C. Bartolozzi, B. Tabata, A. Censi, S. Leutenegger, A. Davison, J. Conradt, K. Daniilidis, and D. Scaramuzza, “Event-based vision: A survey,” *IEEE transactions on pattern analysis and machine intelligence*, vol. PP, jul 2020.
  - [15] C. von der Malsburg, “The correlation theory of brain function,” Tech. Rep. 81-2, Max-Planck-Institute for Biophysical Chemistry, Göttingen, Germany, 1981.
  - [16] C. Von der Malsburg, “Binding in models of perception and brain function,” *Current opinion in neurobiology*, vol. 5, no. 4, pp. 520–526, 1995.
  - [17] D. E. Feldman, “The spike-timing dependence of plasticity,” *Neuron*, vol. 75, pp. 556–571, aug 2012.
  - [18] J.-H. Jacobsen, J. Behrmann, R. Zemel, and M. Bethge, “Excessive invariance causes adversarial vulnerability,” *arXiv preprint arXiv:1811.00401*, 2018.



- [19] T. A. Plate, “Holographic Reduced Representations,” *IEEE Transactions on Neural Networks*, vol. 6, no. 3, pp. 623–641, 1995.
- [20] P. Kanerva, “Binary spatter-coding of ordered k-tuples,” in *Artificial neural networks —ICANN 96* (C. Malsburg, W. Seelen, J. C. Vorbrüggen, B. Sendhoff, G. Goos, J. Hartmanis, and J. Leeuwen, eds.), vol. 1112 of *Lecture notes in computer science*, pp. 869–873, Berlin, Heidelberg: Springer Berlin Heidelberg, 1996.
- [21] R. W. Gayler and R. Wales, “Connections, Binding, Unification and Analogical Promiscuity,” in *Advances in Analogy Research: Integration of Theory and Data from the Cognitive, Computational, and Neural Sciences*, pp. 1–11, 1998.
- [22] R. W. Gayler, “Vector Symbolic Architectures Answer Jackendoff’s Challenges for Cognitive Neuroscience,” in *Joint International Conference on Cognitive Science (ICCS/ASCS)*, pp. 133–138, 2003.
- [23] P. Kanerva, “Hyperdimensional computing: An introduction to computing in distributed representation with high-dimensional random vectors,” *Cognitive computation*, vol. 1, pp. 139–159, jun 2009.
- [24] D. Kleyko, M. Davies, E. P. Frady, *et al.*, “Vector Symbolic Architectures as a Computing Framework for Nanoscale Hardware,” *arXiv:2106.05268*, pp. 1–28, 2021.
- [25] E. Frady, D. Kleyko, C. Kymn, B. Olshausen, and F. Sommer, “Computing on functions using randomized vector representations,” *arXiv preprint arXiv:2109.03429*, 2021.
- [26] E. P. Frady, S. J. Kent, B. A. Olshausen, and F. T. Sommer, “Resonator networks, 1: An efficient solution for factoring high-dimensional, distributed representations of data structures,” *Neural Computation*, pp. 1–21, oct 2020.
- [27] S. J. Kent, E. P. Frady, F. T. Sommer, and B. A. Olshausen, “Resonator networks, 2: Factorization performance and capacity compared to optimization-based methods,” *Neural Computation*, vol. 32, pp. 2332–2388, dec 2020.
- [28] W. Pitts and W. S. McCulloch, “How we know universals the perception of auditory and visual forms,” *The Bulletin of mathematical biophysics*, vol. 9, no. 3, pp. 127–147, 1947.
- [29] G. F. Hinton, “A parallel computation that assigns canonical object-based frames of reference,” in *Proceedings of the 7th international joint conference on Artificial intelligence-Volume 2*, pp. 683–685, 1981.
- [30] B. A. Olshausen, C. H. Anderson, and D. C. Van Essen, “A neurobiological model of visual attention and invariant pattern recognition based on dynamic routing of information,” *Journal of Neuroscience*, vol. 13, no. 11, pp. 4700–4719, 1993.
- [31] D. W. Arathorn, *Map-seeking circuits in visual cognition: A computational mechanism for biological and machine vision*. Stanford University Press, 2002.
- [32] D. Arathorn, “Computation in the higher visual cortices: Map-seeking circuit theory and application to machine vision,” in *33rd Applied Imagery Pattern Recognition Workshop (AIPR’04)*, pp. 73–78, IEEE, 2004.
- [33] J. Tenenbaum and W. Freeman, “Separating style and content,” *Advances in neural information processing systems*, vol. 9, 1996.
- [34] W. T. Freeman and J. B. Tenenbaum, “Learning bilinear models for two-factor problems in vision,” in *Proceedings of IEEE Computer Society Conference on Computer Vision and Pattern Recognition*, pp. 554–560, IEEE, 1997.
- [35] M. A. O. Vasilescu and D. Terzopoulos, “Multilinear analysis of image ensembles: Tensorfaces,” in *European conference on computer vision*, pp. 447–460, Springer, 2002.
- [36] B. A. Olshausen, C. Cadieu, J. Culpepper, and D. K. Warland, “Bilinear models of natural images,” in *Human Vision and Electronic Imaging XII*, vol. 6492, pp. 67–76, SPIE, 2007.
- [37] H. Y. Chau, F. Qiu, Y. Chen, and B. Olshausen, “Disentangling images with lie group transformations and sparse coding,” *arXiv preprint arXiv:2012.12071*, 2020.
- [38] E. P. Frady, D. Kleyko, and F. Sommer, “Variable binding for sparse distributed representations: Theory and applications,” *arXiv preprint arXiv:2009.06734*, 2020.
- [39] M. Davies, N. Srinivasa, T.-H. Lin, G. China, Y. Cao, S. H. Choday, G. Dimou, P. Joshi, N. Imam, S. Jain, *et al.*, “Loihi: A neuromorphic manycore processor with on-chip learning,” *IEEE Micro*, vol. 38, no. 1, pp. 82–99, 2018.
- [40] P. Frady, P. Kanerva, and F. Sommer, “A framework for linking computations and rhythm-based timing patterns in neural firing, such as phase precession in hippocampal place cells,” *CCN*, 2019.
- [41] B. Komer, T. Stewart, A. Voelker, and C. Eliasmith, “A neural representation of continuous space using fractional binding,” in *Annual Meeting of the Cognitive Science Society (CogSci)*, pp. 2038–2043, Cognitive Science Society, 2019.
- [42] D. Kleyko, D. A. Rachkovskij, E. Osipov, and A. Rahimi, “A Survey on Hyperdimensional Computing aka Vector Symbolic Architectures, Part I: Models and Data Transformations,” *arXiv:2111.06077*, pp. 1–27, 2021.
- [43] D. Kleyko, D. A. Rachkovskij, E. Osipov, and A. Rahimi, “A Survey on Hyperdimensional Computing aka Vector Symbolic Architectures, Part II: Applications, Cognitive Models, and Challenges,” *arXiv:2112.15424*, pp. 1–36, 2021.
- [44] T. A. Plate, *Distributed Representations and Nested Compositional Structure*. University of Toronto, PhD Thesis, 1994.
- [45] E. P. Frady, D. Kleyko, and F. T. Sommer, “A theory of sequence indexing and working memory in recurrent neural networks,” *Neural Computation*, vol. 30, pp. 1449–1513, apr 2018.
- [46] J. B. Tenenbaum and W. T. Freeman, “Separating Style and Content with Bilinear Models,” *Neural Computation*, vol. 12, no. 6, pp. 1247–1283, 2000.

- [47] Y. W. Teh, M. Welling, S. Osindero, and G. E. Hinton, “Energy-based models for sparse overcomplete representations,” *Journal of Machine Learning Research*, vol. 4, no. Dec, pp. 1235–1260, 2003.
- [48] T. Kohonen, “An adaptive associative memory principle,” *IEEE Transactions on Computers*, vol. 100, no. 4, pp. 444–445, 1974.
- [49] D. J. Felleman and D. C. Van Essen, “Distributed hierarchical processing in the primate cerebral cortex,” *Cerebral cortex (New York, NY: 1991)*, vol. 1, no. 1, pp. 1–47, 1991.
- [50] E. P. Frady and F. T. Sommer, “Robust computation with rhythmic spike patterns,” *Proceedings of the National Academy of Sciences of the United States of America*, vol. 116, pp. 18050–18059, sep 2019.
- [51] A. Renner, L. Supic, A. Danielescu, G. Indiveri, F. T. Sommer, E. P. Frady, and Y. Sandamirskaya, “Neuromorphic visual odometry with resonator networks,” *arXiv preprint arXiv:2209.02000*, 2022.
- [52] J. Göltz, L. Kriener, A. Baumbach, S. Billaudelle, O. Breitwieser, B. Cramer, D. Dold, A. F. Kungl, W. Senn, J. Schemmel, *et al.*, “Fast and deep: energy-efficient neuromorphic learning with first-spike times,” *arXiv preprint arXiv:1912.11443v4*, 2019.
- [53] I. M. Comsa, T. Fischbacher, K. Potempa, A. Gesmundo, L. Versari, and J. Alakuijala, “Temporal coding in spiking neural networks with alpha synaptic function,” in *ICASSP 2020-2020 IEEE International Conference on Acoustics, Speech and Signal Processing (ICASSP)*, pp. 8529–8533, IEEE, 2020.
- [54] B. Rueckauer and S.-C. Liu, “Conversion of analog to spiking neural networks using sparse temporal coding,” in *2018 IEEE International Symposium on Circuits and Systems (ISCAS)*, pp. 1–5, IEEE, 2018.
- [55] A. Renner, Y. Sandamirskaya, F. T. Sommer, and E. P. Frady, “Sparse vector binding on spiking neuromorphic hardware using synaptic delays,” in *International Conference on Neuromorphic Systems (ICONS 2022)*, ACM, 2022.
- [56] D. Casasent and D. Psaltis, “Position, rotation, and scale invariant optical correlation,” *Applied optics*, vol. 15, no. 7, pp. 1795–1799, 1976.
- [57] Q.-s. Chen, M. Defrise, and F. Deconinck, “Symmetric phase-only matched filtering of fourier-mellin transforms for image registration and recognition,” *IEEE Transactions on pattern analysis and machine intelligence*, vol. 16, no. 12, pp. 1156–1168, 1994.
- [58] B. S. Reddy and B. N. Chatterji, “An fft-based technique for translation, rotation, and scale-invariant image registration,” *IEEE transactions on image processing*, vol. 5, no. 8, pp. 1266–1271, 1996.
- [59] F. Crick and G. Mitchison, “The function of dream sleep,” *Nature*, vol. 304, no. 5922, pp. 111–114, 1983.
- [60] C. R. Vogel, D. W. Arathorn, A. Roorda, and A. Parker, “Retinal motion estimation in adaptive optics scanning laser ophthalmoscopy,” *Optics express*, vol. 14, no. 2, pp. 487–497, 2006.
- [61] C. Geisler, D. Robbe, M. Zugaro, A. Sirota, and G. Buzsáki, “Hippocampal place cell assemblies are speed-controlled oscillators,” *Proceedings of the National Academy of Sciences of the United States of America*, vol. 104, pp. 8149–8154, may 2007.
- [62] N. Burgess, C. Barry, and J. O’Keefe, “An oscillatory interference model of grid cell firing,” *Hippocampus*, vol. 17, no. 9, pp. 801–812, 2007.
- [63] S. Chaudhuri, D. Ritchie, J. Wu, K. Xu, and H. Zhang, “Learning generative models of 3d structures,” in *Computer Graphics Forum*, vol. 39, pp. 643–666, Wiley Online Library, 2020.
- [64] J. Huang and K. Murphy, “Efficient inference in occlusion-aware generative models of images,” *arXiv preprint arXiv:1511.06362*, 2015.